APL Materials

RESEARCH ARTICLE | MAY 12 2025

Multivariate MOF nanozyme utilizes glucose-activated self-cascade strategy for enhanced antibacterial efficacy and accelerated diabetic wounds healing

Yuxin Huang; Dixi Chen; T. M. Wong ; Baolin Li ✉; Yongxin Shi ✉

APL Mater. 13, 051115 (2025)
https://doi.org/10.1063/5.0267620

AIP Publishing

Multivariate MOF nanozyme utilizes glucose-activated self-cascade strategy for enhanced antibacterial efficacy and accelerated diabetic wounds healing

Cite as: APL Mater. 13, 051115 (2025); doi: 10.1063/5.0267620
Submitted: 25 February 2025 • Accepted: 29 April 2025 •
Published Online: 12 May 2025

Yuxin Huang,[1] Dixi Chen,[1] T. M. Wong,[2] Baolin Li,[1,a)] and Yongxin Shi[1,a)]

AFFILIATIONS

[1] Department of Sport Medicine, South China Hospital, Medical School, Shenzhen University, Shenzhen, Guangdong 518116, China
[2] Department of Sport Medicine, Queen Mary Hospital, University of Hong Kong, Hong Kong 999077, China

[a)] **Authors to whom correspondence should be addressed:** libaolin0609@163.com and shiyongxinshi@126.com

ABSTRACT

The impaired immune function observed in diabetic patients significantly increases their susceptibility of diabetic wounds to bacterial infections. Conventional treatment for bacterial infections relies heavily on antibiotics; however, this approach is often accompanied by the development of bacterial resistance. In this study, a nanozyme (Q@CuMn@G) exhibiting exceptional antibacterial efficacy with the capability to circumvent drug resistance was ingeniously designed. It operates through the generation of hydroxyl radicals (•OH) via a self-cascade reaction. The glucose oxidase (GOx) encapsulated within the Cu-metal–organic framework (MOF) generates H_2O_2 by degrading glucose present in the wound environment, which is subsequently catalyzed by the Cu-MOF to produce •OH, thereby exerting potent antibacterial effects. Meanwhile, MnO_2 loaded within Cu-MOF generates O_2, ameliorating the hypoxic environment of the wound and further supporting the degradation of glucose by GOx. Quaternized chitosan is employed as a shell to envelop the nanozyme, thus preventing the rapid degradation of GOx. *In vitro* experiments demonstrated that Q@CuMn@G exhibits sustained release of •OH and significant bactericidal effects against *Escherichia coli* and *Staphylococcus aureus*, confirming the high antibacterial activity of the nanozyme. Moreover, *in vivo* experiments revealed that Q@CuMn@G effectively kills bacteria in infected diabetic wounds, modulates the immune microenvironment, and accelerates wound healing, achieving a healing ratio of 96.78%. This study employs the Q@CuMn@G nanozyme to achieve highly effective antibacterial efficacy through chemodynamic therapy, thereby offering an innovative strategy for antibiotic-free treatment of diabetic wound repair.

I. INTRODUCTION

Chronic wound infections pose a significant challenge to contemporary healthcare, encompassing diabetic wounds, fungal wounds, pressure ulcers, and more.[1,2] The impaired immune function in diabetic patients makes their wounds prone to bacterial infections and hinders their ability to clear such infections autonomously, leading to a disruption in the balance of the immune microenvironment and prolonged inflammatory responses that impede tissue repair.[3,4] However, the overuse of antibiotics in clinical practice has led to the emergence of bacterial resistance, diminishing the efficacy of traditional antibiotics in treating bacterial infections.[5] Consequently, the development of novel therapeutic approaches to circumvent bacterial resistance holds substantial social and economic significance for the treatment of diabetic bacterial-infected wounds.

Chemodynamic therapy (CDT) has been widely applied in the field of antibacterial therapy as a novel treatment strategy in recent years.[6] CDT is predicated on the Fenton/Fenton-like reaction, utilizing Fenton metals-including Fe-based nanocatalysts and various Fenton metalloid nanocatalysts such as Cu, Mn, Mo, and Ag—to convert endogenous H_2O_2 into hydroxyl radicals (•OH) that can effectively eliminate bacteria and circumvent bacterial resistance.[7]

Therefore, CDT involving •OH is regarded as an ideal antibacterial modality.[8–10] Because of their high porosity and large specific surface area, metal–organic frameworks (MOFs), which are composed of nodal metals or metal oxides and organic linker ligands, are chemically stable and serve as effective CDT reagents. When active molecules capable of performing Fenton or Fenton-like reactions are utilized as building blocks of MOFs, they can decompose in acidic environments and achieve antibacterial effects through CDT.[11–13] Among various MOF materials, Cu MOFs are promising CDT reagents. The Cu^+/Cu^{2+} in Cu-MOFs exhibit variable oxidation states, allowing them to catalyze the generation of highly reactive •OH from H_2O_2 through Fenton-like reactions. In addition, Cu-MOFs possess a high specific surface area and well-defined porous structures, facilitating the efficient loading and release of H_2O_2 or other reactants. Furthermore, the organic ligands in Cu-MOFs can be chemically modified to introduce specific functional groups, allowing for the design of more efficient CDT agents tailored to specific requirements.[14–16]

However, the content of endogenous H_2O_2 is often insufficient, restricting the therapeutic efficacy of CDT.[17] To address this limitation, researchers have developed various novel materials. Zhao *et al.*[18] encapsulated Cu–Fe peroxide nanoparticles, which can be decomposed to release substantial quantities of exogenous H_2O_2 under near-infrared (NIR) irradiation, thereby compensating for the limitations of endogenous H_2O_2 and further enhancing the performance of CDT. Wang *et al.*[19] designed a Cu peroxide-loaded mesoporous dopamine nanomaterial (CuO_2@MPDA). This MPDA-mediated photothermal therapy (PTT) can enhance the production of •OH from CuO_2 by accelerating the chemical reactions, thereby demonstrating high antibacterial efficiency at very low concentrations. Although these strategies address the issue of inadequate endogenous H_2O_2 levels, they still rely on external physical stimuli to enhance H_2O_2 generation, introducing additional complexity to wound treatment protocols. For diabetic chronic wounds, adopting a tailored approach—leveraging the hyperglycemic environment to generate H_2O_2—is considered a strategic and effective solution. Glucose oxidase (GOx) can catalyze the oxidation of glucose to generate H_2O_2,[20–23] addressing the issue of insufficient endogenous H_2O_2 for CDT agents in diabetic models. This enzymatic property makes GOx a promising candidate for enhancing the efficacy of CDT in glucose-rich pathological environments. When GOx is combined with Fenton or Fenton-like reagents, the generated H_2O_2 can be further catalyzed to produce highly antibacterial •OH, exerting potent antibacterial effects through a cascading reaction. Simultaneously, this process consumes blood glucose, modulates the immune microenvironment, and accelerates wound healing.

In light of the above-mentioned considerations, a multifunctional nanozyme with potent antibacterial properties specifically targeting diabetic refractory wounds was designed (Scheme 1). Utilizing a well-established hydrothermal synthesis method, we fabricated Cu-MOF@MnO_2 nanocomposites (CuMn), which were subsequently functionalized with GOx via physical adsorption to establish an efficient cascade reaction system. Finally, quaternized chitosan (QCS) was used to encapsulate the nanozyme, preventing premature degradation of GOx (Q@CuMn@G). The GOx loaded on the nanozyme decomposes glucose, generating H_2O_2 and gluconic acid. The Cu MOF catalyzes a Fenton-like reaction, facilitating the decomposition of H_2O_2 to generate highly antibacterial •OH, achieving antibacterial effects through CDT. In addition, MnO_2 decomposes H_2O_2 to produce oxygen, further accelerating wound healing. This innovative design not only addresses the challenges of bacterial infection and hypoxia in diabetic wounds but also provides a cascade-based therapeutic strategy to promote wound healing.

II. EXPERIMENTAL SECTION

A. Materials

Potassium permanganate ($KMnO_4$, AR), sodium thiosulfate ($Na_2S_2O_3$, AR), trimellitic acid (H_3BTC, AR), Cu sulfate pentahydrate ($CuSO_4\cdot 5H_2O$, AR) and quaternized chitosan (QCS, AR) were purchased from Macklin, glucose oxidase (GOx, AR) was purchased from Aladdin, and absolute ethanol was purchased from Damao, Tianjin.

B. Preparation of MnO_2 NPs and CuMn@G

For the preparation of MnO_2 NPs, 50 ml of deionized water is used to dissolve 0.017 g of $KMnO_4$, and the liquid is then sonicated for 30 min. To dissolve 0.017 g of $Na_2S_2O_3$, 50 ml of deionized water was utilized. Drop by drop, the previously prepared $Na_2S_2O_3$ solution was added to the $KMnO_4$ solution at 25 °C, rapidly changing the color of the mixture from purple to yellow-brown. This demonstrated the formation and eventual dark browning of the MnO_2 NPs. After washing with water by centrifugation, the particles were mixed into a 2 ml solution and stored for later use.

For the synthesis of Cu-MOF@MnO_2 (CuMn), 0.45 g (2.14 mM) of H_3BTC was dissolved in 48 ml of anhydrous ethanol under continuous magnetic stirring. Subsequently, 0.75 g (3.1 mM) of $CuSO_4\cdot 5H_2O$ was introduced into the solution, followed by vigorous stirring for 10 min. MnO_2 nanoparticles were then incorporated into the mixture, which was transferred into a Teflon-lined autoclave for hydrothermal treatment at 120 °C for 12 h. After cooling to ambient temperature, the resulting product was collected via centrifugation, washed three times with anhydrous ethanol to remove residual reactants, and dried under vacuum at 60 °C for 24 h, yielding the final CuMn composite.

For the synthesis of Cu-MOF@MnO_2@GOx (CuMn@G), CuMn (20 mg, 4 mg/ml) was mixed with GOx (5 mg, 1 mg/ml) in deionized water and stirred in the dark for 24 h, followed by centrifugation to obtain CuMn@G. Meanwhile, the supernatant before and after GOx adsorption was collected, and the GOx loading capacity was determined using a BCA assay kit.

C. Preparation and characterization of Q@CuMn@G

QCS (10 mg, 2 mg/ml) was added to the CuMn@G (20 mg, 4 mg/ml) composite and stirred continuously for 2 h. The Q@CuMn@G composite was then produced by freeze-drying after a single wash with deionized water. Using scanning electron microscopy (SEM) and transmission electron microscope (TEM), the morphological properties of Cu-MOF, CuMn, and Q@CuMn@G were investigated. To determine the valence states, describe the atomic chemical environments, and carry out peak deconvolution analysis, X-ray photoelectron spectroscopy (XPS) was utilized. X-ray diffraction (XRD) analysis was used to identify the crystallographic facets, which were then compared with reference data for standard MnO_2. Q@CuMn@G was subjected to Fourier-transform

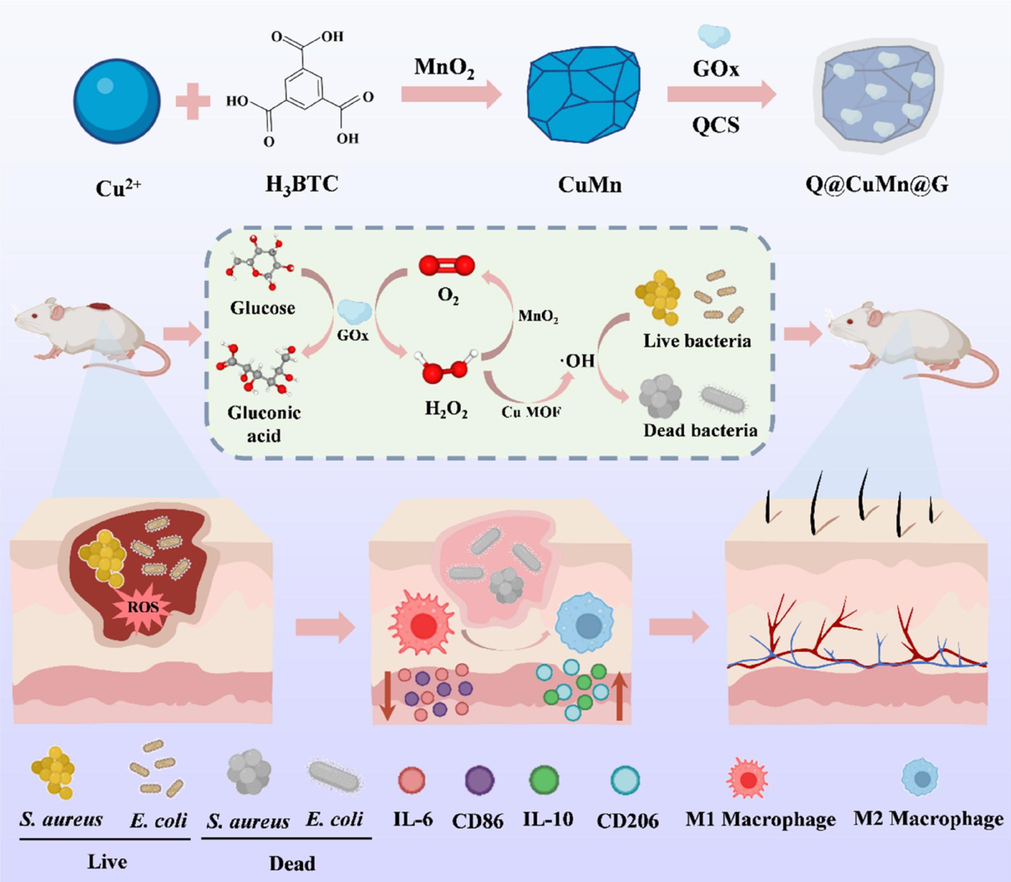

Scheme 1. Fabrication of Q@CuMn@G and the underlying mechanisms mediating enhanced wound healing.

infrared spectroscopy (FT-IR) in order to obtain spectral data in the 4000–500 cm^{-1} range. The Brunauer–Emmett–Teller (BET) method was employed to analyze the surface area and pore size distribution of Cu-MOF, CuMn, and Q@CuMn@G. Q@CuMn@G solution (0.1 mg/ml) was incubated at 37 °C for 48 h, and the cumulative release of Cu^{2+} was quantified using inductively coupled plasma mass spectrometry (ICP-MS) at designated time intervals.

D. Hydroxyl radical detection

The peroxidase-like activity was systematically investigated under various conditions by examining different materials (MnO$_2$, Cu-MOF, CuMn, and Q@CuMn@G) and by modulating the pH and concentration of Q@CuMn@G after incubation with 7.7% H$_2$O$_2$ in advance. The peroxidase-like activity of the samples was quantitatively assessed by measuring the absorbance of TMB at 652 nm and methyl violet at 580 nm.

Reaction mixtures comprising glucose (Glu, 50 mM), Glu with GOx, Glu with CuMn (2 mg/ml), Q@CuMn@G (2 mg/ml), and Glu with Q@CuMn@G were incubated with TMB (6 mM) for 30 min in order to examine the enzymatic activity of GOx. After centrifuging the reactions, the UV absorbance at 652 nm was determined.

E. Oxygen detection

Q@CuMn@G was immersed in a solution (pH 6) for different times; the supernatant was discarded after centrifugation, and then H$_2$O$_2$ solution (pH 7.4, 0.25 M) was added to observe the number of bubbles formed.

F. Assessment of antibacterial activity *in vitro*

Using *Staphylococcus aureus* (*S. aureus*) and *Escherichia coli* (*E. coli*), evaluating the antibacterial efficiency of the different treatment groups. After adjusting the bacterial suspension to a concentration of 10^7 CFU/ml, it was divided into four experimental groups and supplemented with Glu (1 M) and Cu-MOF, CuMn, and Q@CuMn@G (all at 2 mg/ml). The samples underwent incubation at 37 °C with 200 rpm agitation, and the optical density (OD) of the bacterial solutions was measured at predefined intervals.

G. Cell testing *in vitro*

1. The CCK-8 assay and cell live/dead staining

To determine the biocompatibility of extracts from different materials, human umbilical vein endothelial cells (HUVECs) were cultivated with them. After being sown on 96-well plates, HUVECs were left in material extracts for 24 and 48 h. The vitality of the cells was assessed using the cell counting kit-8 (CCK-8) and live/dead cell staining. A fluorescent microscope was used to visualize cellular fluorescence, and a microplate reader was used to determine OD values.

2. Crystal violet staining

After fixing the cells with 4% paraformaldehyde, they were rinsed with PBS to get rid of any leftover fixative, and then they were stained for 15 min with 0.1% crystal violet. The cells were stained, washed with deionized water to get rid of any remaining dye, and then photographed under an optical microscope.

3. Cytoskeleton staining

For 24 h, HUVEC and material extracts were co-cultured. FITC-conjugated phalloidin was then used to stain F-actin, and DAPI was used to counterstain the cell nuclei. From then on, fluorescence microscopy was used to visualize cellular morphology.

4. In vitro scratch assay

HUVECs were cultivated until 90% confluency after being sown in 24-well plates at a density of 4×10^4 cells/well. Then, sterile pipette tips were used to generate a consistent scratch wound. Following the addition of material extracts to the wells, the cells were co-cultured for 48 h. Phase-contrast microscopy was used to capture images and track cell migration at predetermined intervals.

5. Transwell assay

A 24-well plate was used to hold the logarithmic growth phase HUVEC, which were seeded at a density of 3×10^4 cells/well into the upper chamber of transwell inserts. Serum-free medium was maintained in the upper chamber, while complete medium with 20% FBS added was placed in the lower chamber. After 24 h of incubation, the medium was taken out, and 0.1% crystal violet staining was used to measure the number of migrating cells.

6. Cellular immunofluorescence

HUVEC and RAW264.7 macrophages from various treatment groups were blocked with 5% BSA for 1 h at 25 °C after being fixed with 4% paraformaldehyde and permeabilized with Triton X-100 (0.1%). Primary antibodies against HIF-1, CD86, and CD206 were then added to the cells and incubated for 1 h at 37 °C. Next, unbound antibodies were rinsed with PBS, and then fluorophore-conjugated secondary antibodies were added and left to incubate for 1 h in the dark. The cell nuclei were counterstained with DAPI, and fluorescence images were captured using a confocal microscope.

H. Hemolysis assays

Fifty microliter material suspensions were incubated with 1 ml of saline at 37 °C for 30 min, while saline without nanozyme and 1 ml of deionized water were used as positive and negative controls, respectively. Each experimental group then received 20 μl of freshly drawn rat arterial blood, which was then incubated at 37 °C for 1 h. Following centrifugation, spectrophotometry was used to detect the supernatant's absorbance at 545 nm.

I. The wound model of diabetic rats was established *in vivo*

A diabetic wound healing model was established in Sprague–Dawley (SD) rats. Streptozotocin (65 mg/kg) was intraperitoneally injected 5 days prior to wound induction. Diabetes induction was confirmed through consecutive blood glucose measurements (>300 mg/dl). Rats were then anesthetized with sodium pentobarbital (50 mg/kg), and a full-thickness excised bacterial infected wound (10 mm diameter) was created on the dorsal surface following aseptic preparation. Wounds were topically treated with PBS, Cu-MOF, CuMn, and Q@CuMn@G daily. Wound healing progression was documented through digital photography at postoperative days 0, 3, 7, 10, and 14. Wound areas were quantified using ImageJ software. The animal studies were sanctioned by the Medical Ethics Committee of Guangzhou Maiersi Biotechnology Co., LTD. (IACUC-MIS20230171-1) and were carried out strictly by the operating procedures of the Animal Center.

J. Histological and immunohistochemical analysis

On the 14th postoperative day, the animals were put to sleep, and samples of wound tissue were taken for histological examination. Skin samples were fixed, embedded, and dehydrated and then sectioned at a thickness of 4 μm. Immunofluorescence staining for CD31 and α-smooth muscle actin (α-SMA), Masson's trichrome staining, and H&E staining were used for histological analysis. We used both light and fluorescence microscopy to evaluate stained sections.

K. Statistical analysis

The mean ± SD is used to express all experimental results. The *t*-test or one-way analysis of variance (ANOVA) was used for the statistical analyses, and the significance levels were $^{*}p < 0.05$, $^{**}p < 0.01$, and $^{***}p < 0.001$.

III. RESULTS AND DISCUSSION

A. Representation of Q@CuMn@G

The crystal structures of Cu-MOF, CuMn, and Q@CuMn@G were systematically characterized by XRD, with the corresponding diffraction patterns shown in Fig. 1(d). Comparison with the simulated XRD pattern of Cu-MOF (Figure S1) confirmed the formation of highly purified Cu-MOF. Significant alterations in diffraction peaks were observed upon MnO_2 doping in Cu-MOF. The comparative analysis of the XRD pattern with the standard reference for α-MnO_2 (JCPDS PDF#43–1455) revealed excellent correspondence between the observed diffraction peaks and the characteristic (101), (201), (211), (410), (402), and (103) crystallographic planes. This confirms the successful formation of Mn-doped Cu-MOF (CuMn). The XPS survey spectrum of Cu-MOF, CuMn, and Q@CuMn@G [Fig. 1(a)] exhibited distinct peaks corresponding to Cu 2p, Mn 2p, O 1s, N 1s, and C 1s core levels. Furthermore, the high-resolution Cu 2p spectrum of Cu-MOF exhibits distinct peaks at 935.0 and 954.9 eV [Fig. 1(b)], corresponding to Cu $2p_{3/2}$ and Cu $2p_{1/2}$ transitions, respectively. These spectral signatures confirm the predominant presence of Cu^{2+} species in the MOF structure. Similarly, the Mn 2p spectrum reveals two characteristic components at 642.9 eV (Mn $2p_{3/2}$) and 651.2 eV (Mn $2p_{1/2}$)

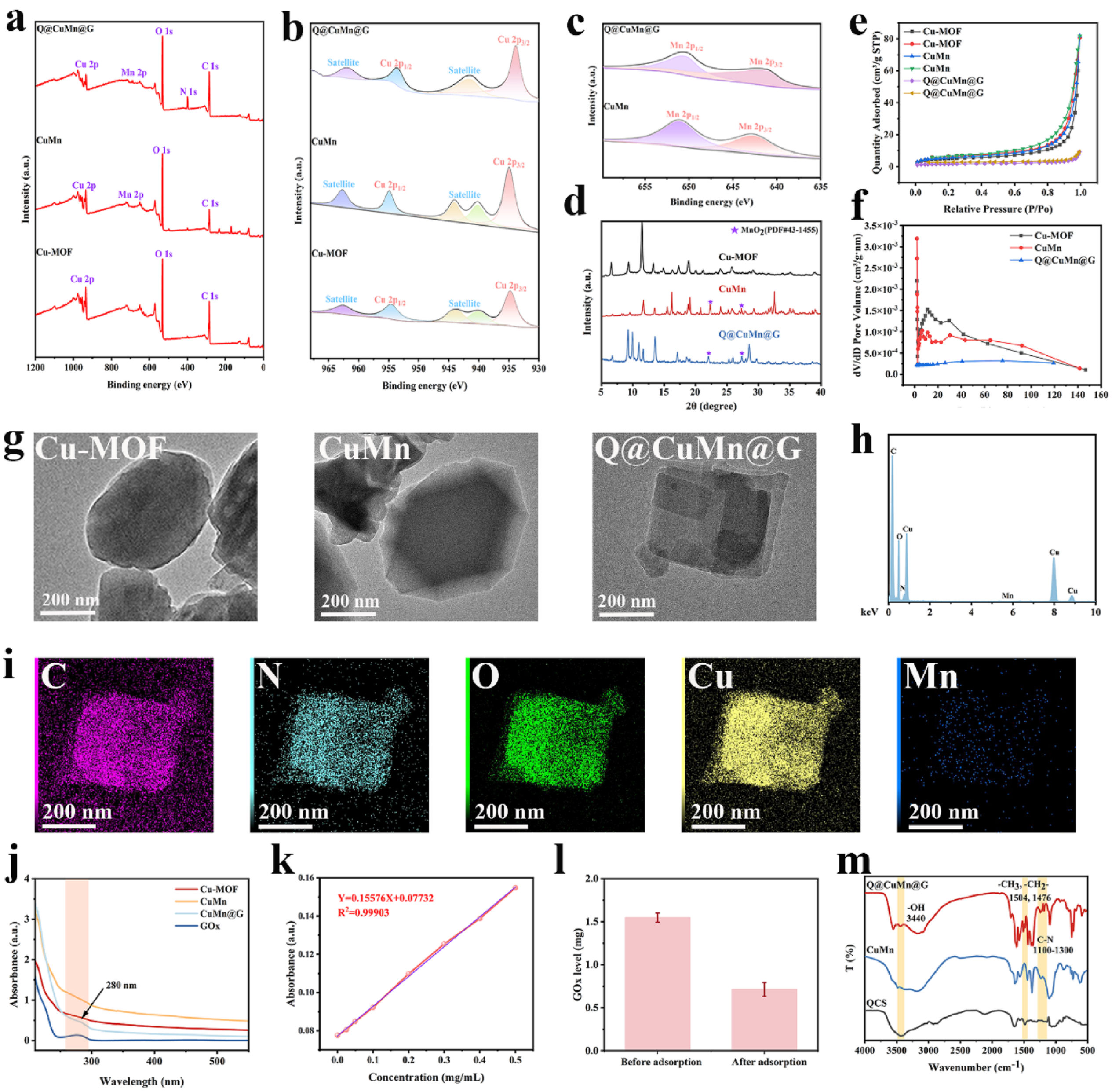

FIG. 1. Characterization of Q@CuMn@G NPs. (a) XRD patterns of Cu-MOF, CuMn, and Q@CuMn@G. (b) and (c) High-resolution Cu2p and Mn2p spectra of Cu-MOF, CuMn, and Q@CuMn@G. (d) XRD spectra of Cu-MOF, CuMn, and Q@CuMn@G. (e) Nitrogen adsorption desorption curve and pore diameter distribution (f) of Cu-MOF, CuMn, and Q@CuMn@G. (g) TEM images of Cu-MOF, CuMn, and Q@CuMn@G. (h) EDS spectrum of Q@CuMn@G. (i) Elemental mapping of C, N, O, Cu, and Mn of Q@CuMn@G. (j) UV–vis spectra of Cu-MOF, CuMn, CuMn@G, and GOx. (k) Standard curves for BCA protein quantification. (l) Protein quantification of GOx before and after adsorption. (m) FTIR spectra of various materials.

[Fig. 1(c)], providing definitive evidence for the successful incorporation of MnO_2. This isotherm is classified as Type III according to the IUPAC classification, accompanied by an H3 hysteresis loop [Fig. 1(e)]. Due to the loading of GOx and encapsulation by the outer chitosan layer, the pore size of Q@CuMn@G became smaller compared to CuMn [Fig. 1(f)], indicating the effective loading of GOx and the successful encapsulation of QCS. SEM analysis (Figure S2) demonstrated that Q@CuMn@G exhibited a well-defined layered morphology throughout the synthesis process. As demonstrated by TEM [Fig. 1(g)], the particle sizes of Cu-MOF, CuMn, and Q@CuMn@G were nearly identical, and elemental mapping confirmed the homogeneous distribution of constituent elements.

The detection of nitrogen signals was attributed to the presence of both QCS and GOx [Figs. 1(h) and 1(i)]. The successful immobilization of GOx in CuMn@G was confirmed by the UV–vis spectrum [Fig. 1(j)], which showed a distinctive absorption peak at 280 nm.[24] The loading efficiency of GOx was quantitatively determined through the BCA protein assay. Prior to and following adsorption, the amount of protein in the supernatant was determined [Fig. 1(l)], with reference to a pre-established protein quantification standard curve [Fig. 1(k)], yielding a calculated GOx loading efficiency of 53.98%.[16] FT-IR analysis of Q@CuMn@G [Fig. 1(m)] revealed characteristic absorption bands at 3440 cm^{-1} (O–H), 1504 and 1476 cm^{-1} (C–H), and 1100–1300 cm^{-1} (C–N), confirming the successful incorporation of QCS functional groups. The above-mentioned series of characterization results proved that Q@CuMn@G was successfully synthesized. To ensure the efficacy and safety of the nanozyme, the release of copper ions from Q@CuMn@G was monitored using ICP-MS (Figure S3). The results indicated that the cumulative release of Cu^{2+} reached ~0.2 mg/l within 48 h, which remained within safe limits.[25]

B. *In vitro* self-cascade reaction of Q@CuMn@G

Cu, as a Fenton-like active metal, catalyzes the conversion of endogenous H_2O_2 into •OH via Fenton-like reactions, while GOx facilitates the enzymatic catabolism of glucose to generate H_2O_2. The POD-like catalytic mechanism involves the decomposition of H_2O_2 coupled with the oxidation of TMB to form a blue-colored product, enabling quantitative assessment of enzymatic activity through spectrophotometric measurement of the characteristic absorbance. Consequently, we quantitatively assessed the enzymatic activity of GOx within the composite materials by detecting •OH. The results [Fig. 2(a)] indicate that H_2O_2 is only produced when both glucose and GOx are present, and that H_2O_2 generates •OH in the presence of Cu-MOF. Under the intervention of H_2O_2, the generation abilities of •OH from different products were observed. It was visually evident that the production of •OH is mainly attributed to the catalytic capability of Cu-MOF [Fig. 2(b)]. Subsequently, a quantitative analysis was conducted, revealing no significant differences in catalytic performance among Cu-MOF, CuMn, and Q@CuMn@G [Fig. 2(c)]. We further investigated the POD-like catalytic behavior of Q@CuMn@G under various experimental conditions. As illustrated in Fig. 2(d), the POD-like activity of Q@CuMn@G exhibited a pH-dependent enhancement, with catalytic efficiency progressively increasing as the pH decreased. This phenomenon can be attributed to the pH-responsive decomposition of Cu-MOF, where lower pH values promote increased release of Cu^{2+}, thereby enhancing the POD-like catalytic activity. The concentration-dependent POD-like activity of Q@CuMn@G was systematically evaluated, as presented in Figs. 2(e) and 2(f). The concentration of Q@CuMn@G and its POD-like enzymatic activity were positively correlated [Fig. 2(e)]. Methyl violet, which exhibits a purple color in its reduced state, undergoes substrate-mediated oxidation to a colorless form in the presence of POD-like activity. The experimental data presented in Fig. 2(f) further corroborate that elevated concentrations of Q@CuMn@G significantly enhance the POD-like enzymatic activity. Furthermore, we employed an alternative approach to evaluate the POD-like activity of CuMn through quantitative measurement of oxygen evolution. As illustrated in Fig. 2(g), with the increase in the acid treatment time of Q@CuMn@G, the reaction process was accelerated, promoting MnO_2 to catalyze the production of O_2 from H_2O_2, indicating an enhanced catalytic activity of CAT-like activity in Q@CuMn@G after acid treatment. To further investigate the stability of GOx in Q@CuMn@G, we measured its catalytic activity over a 5-day period (Figure S4). The results revealed that while GOx activity exhibited a declining trend during this timeframe, it maintained measurable catalytic activity throughout the observation period. Figure 2(h) presents a comprehensive reaction pathway schematic, elucidating the mechanistic details of the catalytic processes within the system: GOx reacts with glucose to produce H_2O_2, catalyzed by Cu-MOF to form •OH. MnO_2 catalyzes H_2O_2 to generate O_2, supporting glucose breakdown by GOx in a cascade reaction.

C. Antibacterial activity of Q@CuMn@G

The aforementioned experimental findings demonstrate the efficient cascade catalytic properties of Q@CuMn@G. Consequently, this system not only depletes essential bacterial nutrients such as glucose but also converts the generated H_2O_2 into •OH through catalytic processes, thereby achieving potent antibacterial effects.[26] To systematically evaluate the antibacterial efficacy of Q@CuMn@G, the growth curves of bacteria were initially determined [Figs. 3(a) and 3(b)], and a 12-h time point was selected as the intervention duration for subsequent plate validation experiments. The antibacterial activity of Q@CuMn@G was quantitatively assessed using the spread plate method, with the results presented in Fig. 3(c). Both CuMn and Q@CuMn@G exhibited relatively low antibacterial activity, whereas Q@CuMn@G demonstrated significant antibacterial activity after glucose culture. Its potent antibacterial performance can be attributed to GOx-mediated oxidation of glucose to generate H_2O_2, as well as the Fenton-like reaction catalyzed by Q@CuMn@G to decompose H_2O_2, thereby releasing •OH to eradicate bacteria. To validate this conclusion, vitamin C was added to the Q@CuMn@G + Glu group to scavenge •OH, resulting in weakened bactericidal efficacy in this group. This confirms that the antibacterial effect of Q@CuMn@G is mediated by the production of •OH (Figure S5). Furthermore, the antibacterial mechanism was corroborated through SEM analysis. As shown in Fig. 3(d), the bacterial membrane integrity was severely disrupted following treatment with Q@CuMn@G in the presence of Glu, providing direct visual evidence of the material's potent antibacterial properties.

D. Biocompatibility of Q@CuMn@G

Biocompatibility represents a crucial parameter for assessing the clinical applicability of nanozyme materials.[27] The cellular viability of HUVEC co-cultured with various materials was quantitatively assessed using Live/Dead staining at specific time points. The Cu-MOF, CuMn, and Q@CuMn@G groups showed a progressive increase in cell density and a much lower cellular mortality rate than the normal group. Crystal violet staining assays further confirmed enhanced proliferative activity in HUVEC following material treatment, shown in Fig. 4(a). Quantitative cell viability analysis revealed that the Q@CuMn@G group demonstrated superior proliferative capacity compared to other groups, with viability exceeding 100% [Fig. 4(b)]. Cellular morphology was examined through cytoskeletal staining using FITC-conjugated phalloidin.[28] Morphological analysis [Fig. 4(c)] demonstrated that HUVECs cultured

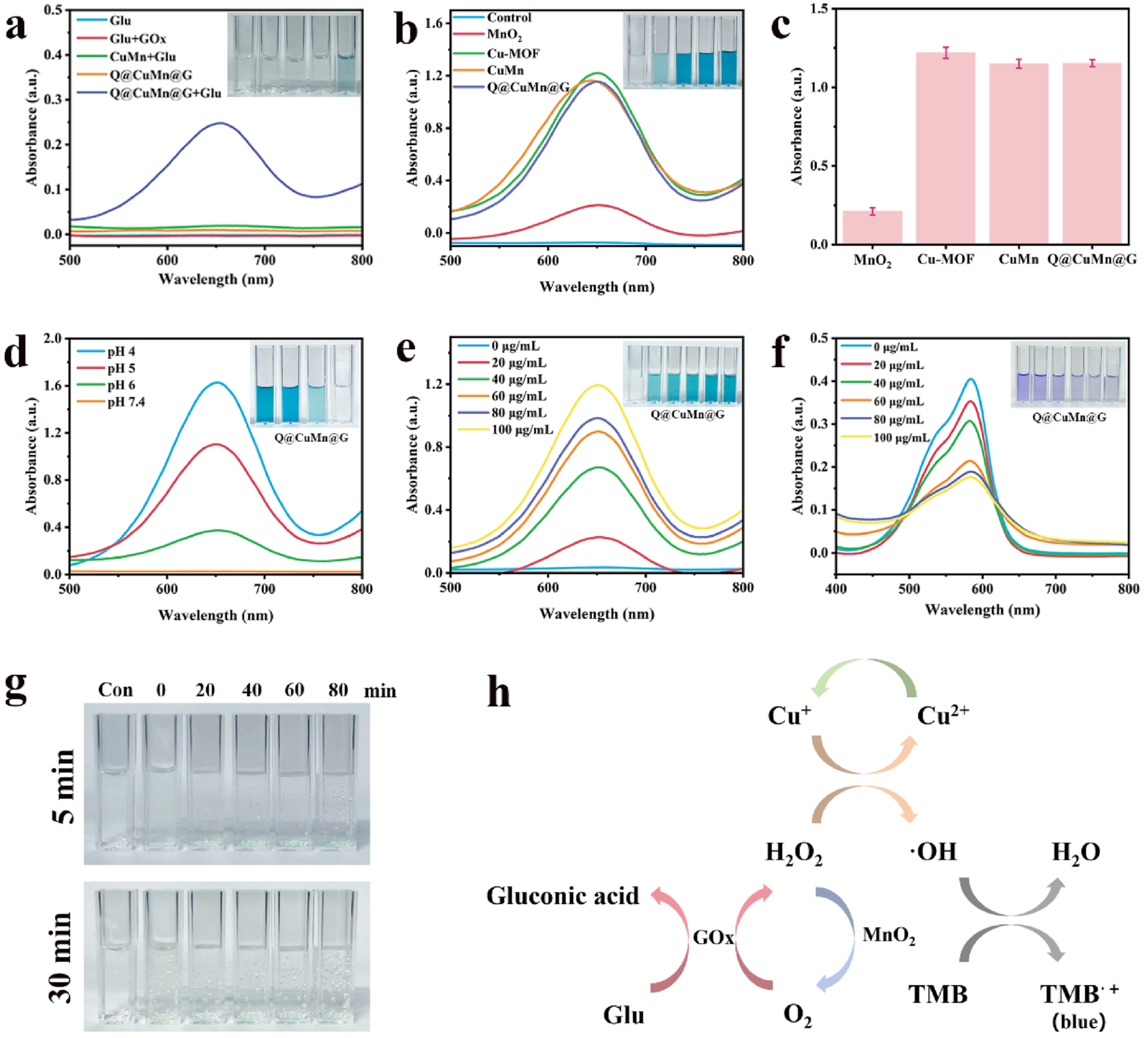

FIG. 2. *In vitro* self-cascade reaction of Q@CuMn@G. (a) Assay of GOx activity. (b) POD-like activity of different substances. (c) Quantification of absorbance values of POD-like activity for different substances. (d) POD-like activity of Q@CuMn@G at different pH; the Q@CuMn@G concentration was 100 μg/ml. (e) POD-like activity of Q@CuMn@G at different concentrations was detected by TMB. (f) POD-like activity of Q@CuMn@G at different concentrations was detected by methyl violet. (g) CAT-like activity of Q@CuMn@G after acid treatment for different times. In the experimental setup, "Con" denotes the Cu-MOF control group, with the upper axis indicating the duration of acid treatment (pH 6) and the left axis representing the reaction time. (h) Schematic representation of the reaction pathway.

with Q@CuMn@G exhibited enhanced cellular spreading and maintained distinct spindle-shaped morphology in comparison to other groups. The hemocompatibility of Q@CuMn@G was assessed using *in vitro* hemolysis experiments. All experimental groups had coloration similar to the negative control, shown in Fig. 4(d), with little hemolytic activity. Notably, the hemolysis ratio in the Q@CuMn@G group remained below 5%, which was within the prescribed hemolysis limit.[29] Furthermore, concentration-dependent hemolysis analysis of Q@CuMn@G [Fig. 4(e)] revealed that concentrations below 100 μg/ml maintained excellent biocompatibility. Cellular migration capacity was evaluated using the *in vitro* wound healing scratch assay.[30] As demonstrated in Fig. 4(f), all treatment groups exhibited

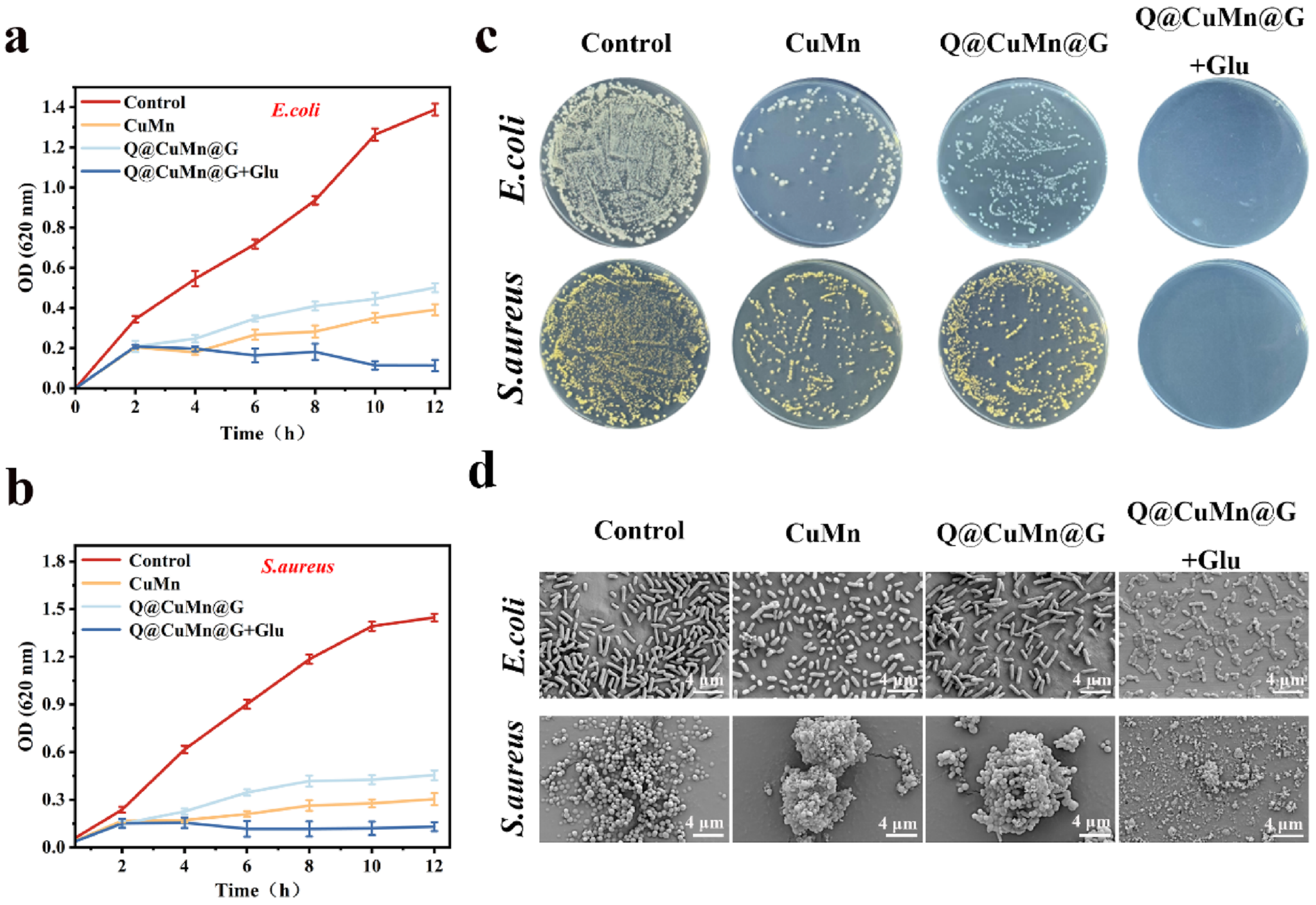

FIG. 3. Antibacterial activity of Q@CuMn@G. (a) *E. coli* and (b) *S. aureus* growth curves for bacteria. (c) Spread plate image illustrates the elimination of *S. aureus* and *E. coli* using several materials (PBS, CuMn, Q@CuMn@G, and Q@CuMn@G + Glu) during a 12-h treatment period. (d) SEM morphology of *S. aureus* and *E. coli* treated with several materials for 12 h.

enhanced migratory capability compared to the model group, with Q@CuMn@G displaying wound closure rates similar to the normal group [Fig. 4(g)]. Complementary Transwell migration assays [Fig. 4(h)] confirmed that Cu-MOF, CuMn, and Q@CuMn@G significantly enhanced HUVEC migration compared to the model group, shown in Fig. 4(i). In summary, Q@CuMn@G exhibits excellent biocompatibility and has significant potential for application in the treatment of diabetic wounds.

E. Immunomodulatory activity of Q@CuMn@G

Since persistent inflammatory responses significantly impair wound healing processes, we systematically evaluated the immunomodulatory potential of Q@CuMn@G. As demonstrated in Figs. 5(a) and 5(e), Q@CuMn@G effectively modulated the immune microenvironment and restored cellular viability following hypoxia and high-glucose treatment. The anti-inflammatory efficacy of Q@CuMn@G was assessed through immunofluorescence analysis. Immunofluorescence results [Fig. 5(b)] revealed significant upregulation of HIF-1 expression in the model group following hypoxia and high-glucose conditions. Treatment with various materials led to HIF-1 downregulation, with Q@CuMn@G demonstrating the most pronounced effect [Fig. 5(f)]. These results are hypothesized to result from the decomposition of glucose by GOx in Q@CuMn@G, generating H_2O_2, which is subsequently catalyzed by MnO_2 to produce O_2, thereby alleviating the cellular damage induced by the hypoxic and high-glucose environment. To investigate Q@CuMn@G-mediated macrophage polarization, we induced M1 and M2 phenotypes using LPS and IFN-γ, followed by immunofluorescence characterization, as presented in Figs. 5(c) and 5(d). The model group showed considerable downregulation of CD206 (M2 marker) and marked elevation of CD86 (M1 marker) expression compared to the normal group. The different material treatments effectively downregulated the expression of CD86 [Fig. 5(g)] while significantly enhancing the expression of CD206 [Fig. 5(h)], with Q@CuMn@G having the most significant effect. This finding indicates that Q@CuMn@G mediates anti-inflammatory effects through inhibiting M1 macrophage polarization and promoting M2 phenotype differentiation.

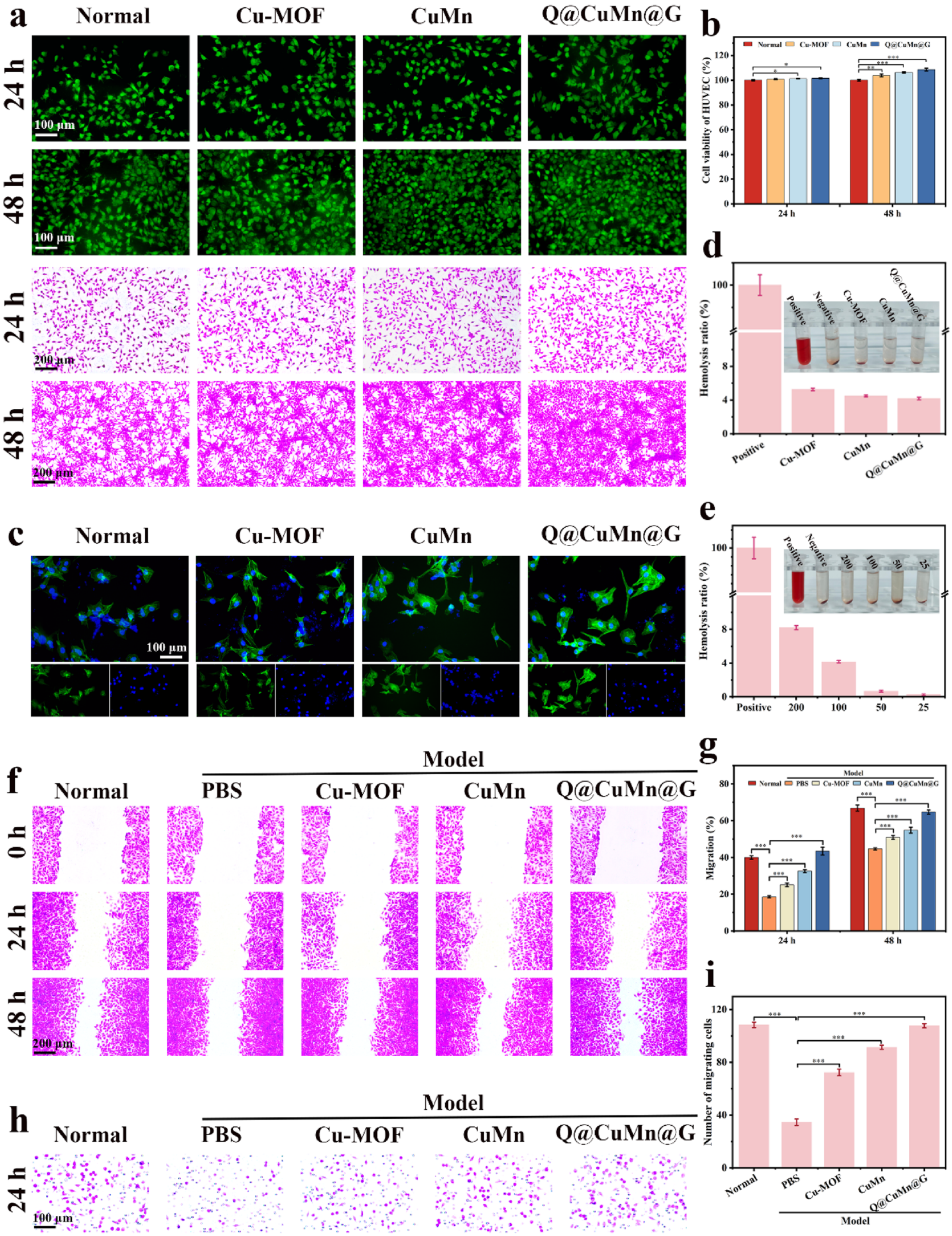

FIG. 4. Biocompatibility of Q@CuMn@G. (a) HUVEC cells treated with different materials for different times were stained with live/dead fluorescence and crystal violet. (b) The CCK-8 assay was used to evaluate cell viability. (c) The adhesion morphology CLSM images at 24 h for various groups. (d) Hemolysis ratio and images of hemolysis for different material treatments. (e) Hemolysis ratio and images of hemolysis treated with different concentrations (μg/ml) of Q@CuMn@G. (f) Pictures of various groups' *in vitro* scratch assays and (g) quantitative analysis. (h) Images of various groups' *in vitro* transwell assays and (i) quantitative analysis.

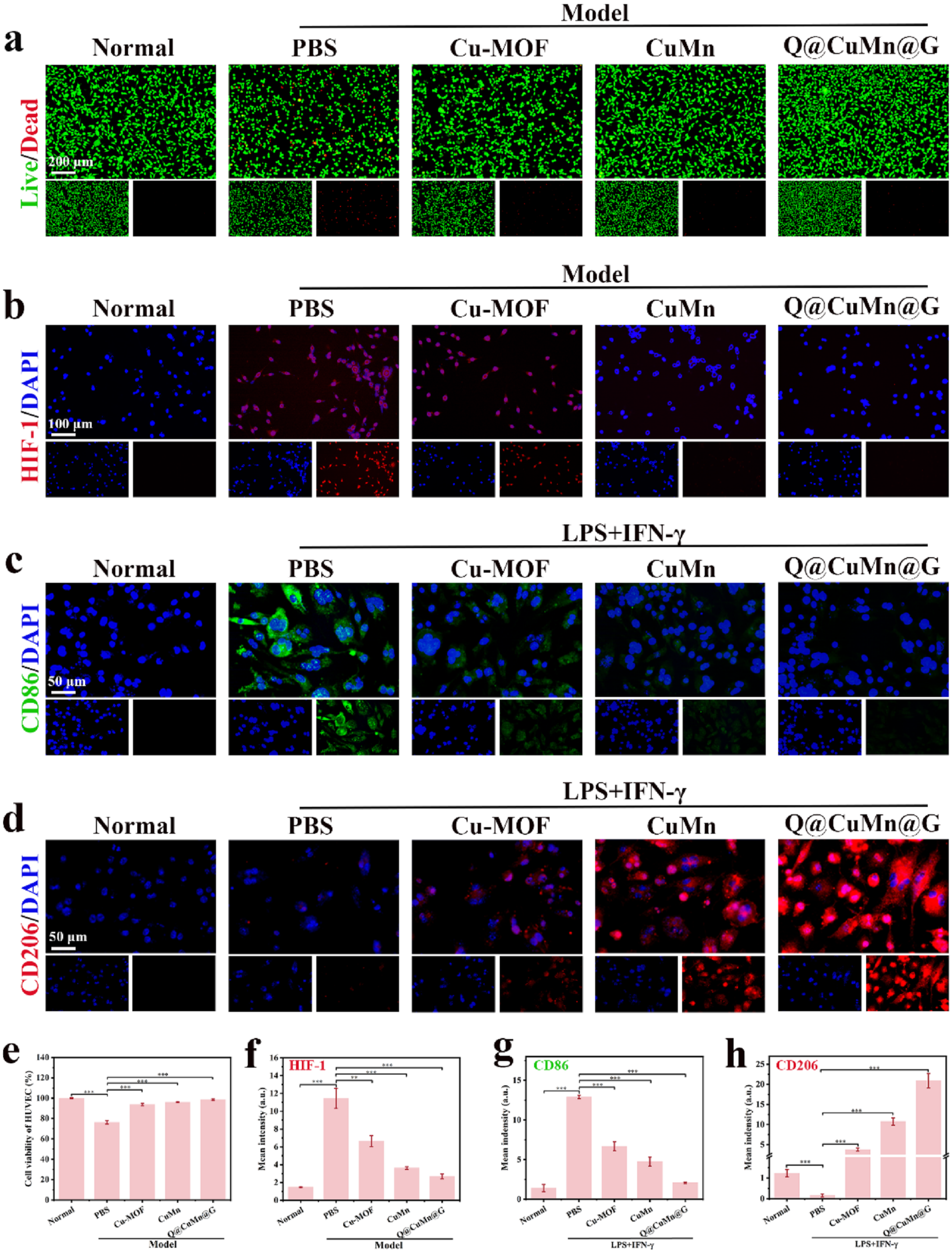

FIG. 5. Immunomodulatory activity of Q@CuMn@G. (a) After the hypoxia and high glucose model, HUVEC cells treated with various substances were stained live or dead. (b) Expression of HIF-1 in HUVEC cells treated with different materials after hypoxia and high glucose modeling and (f) quantitative statistics. (c) CD86 expression in RAW264.7 cells treated with various substances following LPS + IFN-γ modeling and (g) quantitative statistics. (d) CD206 expression in RAW264.7 cells treated with various substances following LPS + IFN-γ modeling and (h) quantitative statistics. (e) Viability of HUVEC cells treated with different materials after hypoxia and high glucose modeling.

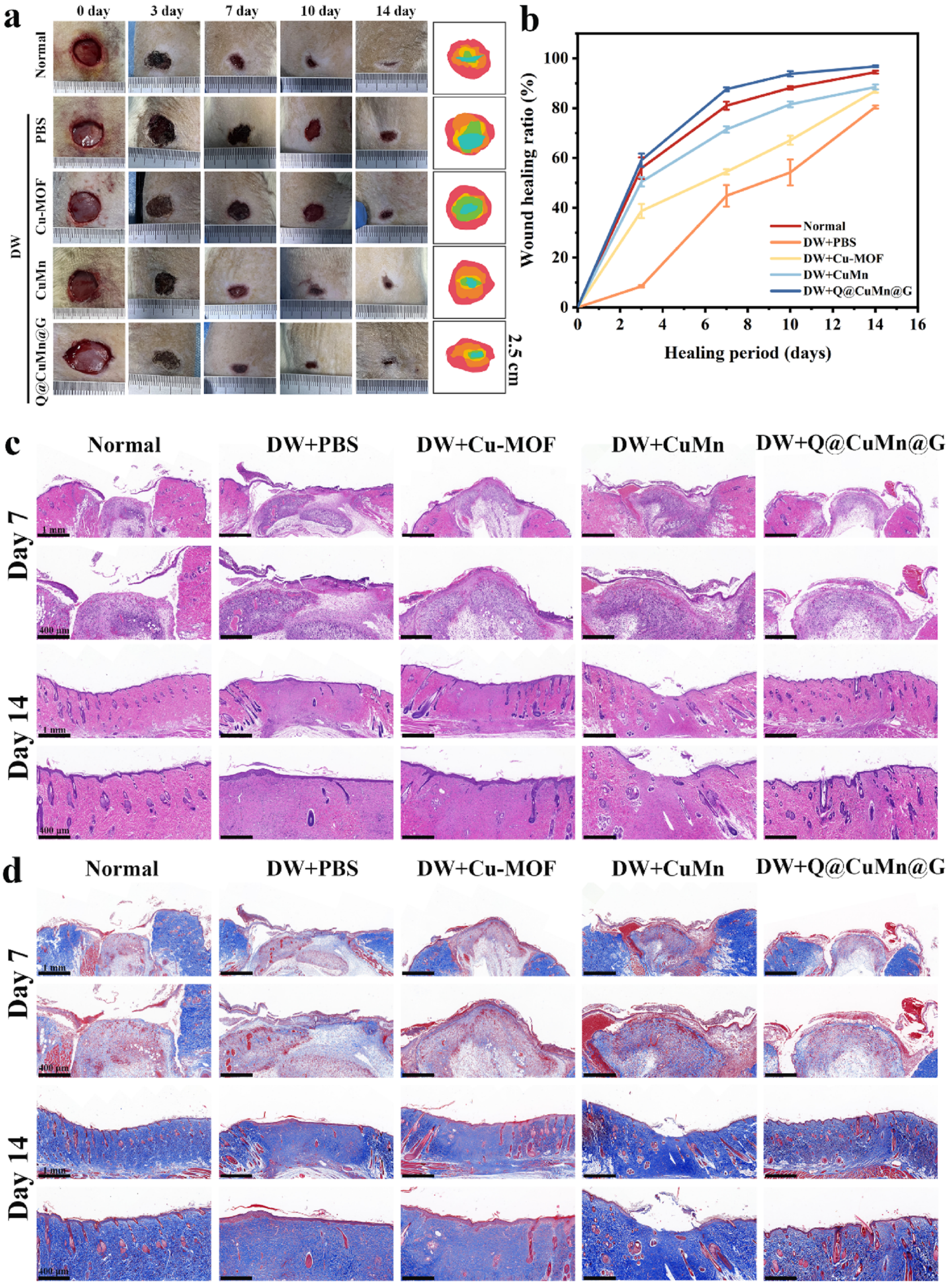

FIG. 6. *In vivo* therapeutic efficacy of Q@CuMn@G. (a) Images of wound healing and wound superpositions at various intervals following treatment with various substances. (b) Statistical analysis of the wound healing ratio over time in various groups. (c) H&E staining at 7 and 14 days in different interventions. (d) Masson staining at 7 and 14 days in different interventions.

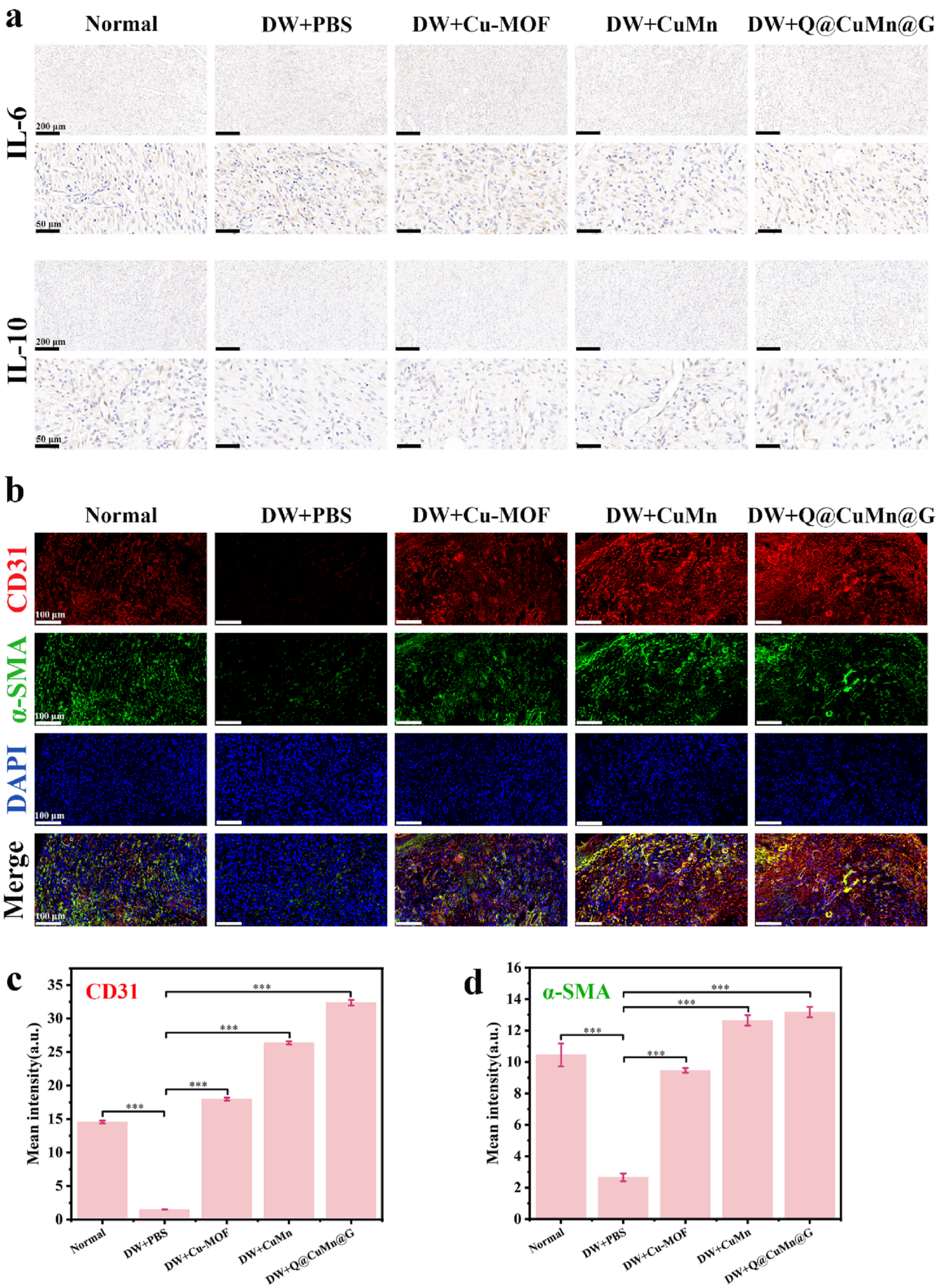

FIG. 7. Angiogenic effects of Q@CuMn@G. (a) Images of immunohistochemical staining for IL-6 or IL-10 (brown). (b) CD31 and α-SMA IF staining in various groups. (c) Quantitative analysis of CD31 and (d) α-SMA expression in various groups.

F. Q@CuMn@G accelerates healing of diabetic infected wounds

To assess Q@CuMn@G's therapeutic effectiveness on diabetic wounds infected with bacteria, we established a full-thickness cortical infected wound model in diabetic rats under anesthesia,[31] which were randomly divided into four experimental groups. As illustrated in Fig. 6(a), all three treatment groups demonstrated significantly enhanced wound healing efficacy compared to the diabetic model group, with visible improvements from day 3 post-treatment. The Q@CuMn@G group exhibited no signs of infection or erythema throughout the healing process, achieving a remarkable wound closure ratio of 96.78% by day 14 [Fig. 6(b)]. This exceptional performance can be attributed to the synergistic catalysis of Q@CuMn@G, where GOx-mediated glucose consumption generates H_2O_2 at the wound site. Subsequently, Cu^{2+} and MnO_2 sequentially catalyze the decomposition of H_2O_2 to produce oxygen and •OH, thereby exerting potent antibacterial effects.[32]

We performed histological studies utilizing Masson's trichrome staining and H&E staining of the skin at the wound site in rats. This was performed to better understand the wound healing mechanisms of Q@CuMn@G. Results are presented in Figs. 6(c) and 6(d). H&E staining analysis revealed that by day 7, inflammatory processes and infection compromised perifollicular vasculature, resulting in significant erythrocyte extravasation. Consequently, the diabetic wound (DW) group exhibited severe erythrocyte aggregation within hair follicles, while all three treatment groups showed significant reduction in this pathological feature compared to the DW group. By day 14, the normal group demonstrated near-complete epidermal regeneration with restored follicular density. Among the treatment groups, Q@CuMn@G demonstrated the highest hair follicle regeneration, indicating superior regenerative capacity. Epidermal thickness measurements [Fig. 6(c)] revealed significant hyperplasia in the DW and DW + Cu-MOF groups compared to normal controls, indicating persistent inflammation, whereas CuMn and Q@CuMn@G groups maintained normal epidermal thickness profiles. Masson's trichrome staining [Fig. 6(d)] demonstrated reduced and disorganized collagen fiber deposition in the DW and DW + Cu-MOF groups, while the Q@CuMn@G group exhibited abundant and densely organized collagen matrix. Q@CuMn@G accelerates diabetic wound healing by promoting hair follicle and epidermal regeneration and increasing collagen deposition.

G. Q@CuMn@G promotes the transition of diabetic infected wounds from the inflammatory to the proliferative stage

Three successive phases, the inflammatory, proliferation, and remodeling phases, generally define the physiological process of cutaneous wound healing. In diabetic bacterial-infected wounds, persistent inflammatory responses prolong the overall healing time.[33] To investigate the immunomodulatory effects of Q@CuMn@G, we performed immunohistochemical analysis of key inflammatory mediators [Fig. 7(a)]. The immunohistochemical analysis revealed that the DW group showed reduced levels of IL-10 and increased levels of IL-6. Q@CuMn@G showed a considerable downregulation of IL-6 expression and an elevation of IL-10 expression when compared to other treatment groups. These findings suggest that Q@CuMn@G exerts potent anti-inflammatory effects by modulating the inflammatory phase of diabetic wound healing, thus accelerating the overall healing process.

Impaired local angiogenesis during the proliferative phase represents another critical factor contributing to delayed healing in diabetic infected wounds.[34,35] Efficient re-epithelialization during the proliferative phase is a crucial determinant of successful wound healing. During the inflammatory phase, fibroblasts are recruited to the wound bed, where they become activated in a low-stress microenvironment, proliferating and secreting collagen matrix components. The production of vital extracellular matrix (ECM) proteins by α-SMA-positive myofibroblasts, such as collagen and fibronectin, aids in wound contraction and encourages tissue remodeling and repair.[36] To assess neovascularization and tissue regeneration, we performed immunofluorescence staining using CD31 and α-SMA as molecular markers [Fig. 7(b)]. According to quantitative examination of fluorescence intensity, all treatment groups exhibited significantly higher levels of CD31 and α-SMA protein than the DW group, with the Q@CuMn@G group displaying the most pronounced upregulation [Figs. 7(c) and 7(d)]. This indicates that Q@CuMn@G promotes neovascularization and wound recovery by upregulating these key markers.

IV. CONCLUSION

In this work, we developed a nanozyme, Q@CuMn@G, which utilizes a glucose-activated self-cascading reaction to achieve efficient antibacterial effects, modulate the immune microenvironment of diabetic wounds, and enable repair of bacterial-infected diabetic wounds. The GOx in Q@CuMn@G reacts with glucose in the wound to generate H_2O_2. The Cu-MOF catalyzes the conversion of H_2O_2 into highly bactericidal •OH through a Fenton-like reaction. Simultaneously, the loaded MnO_2 catalyzes H_2O_2 to produce O_2, alleviating the hypoxic conditions of the wound and further supporting the catalytic activity of GOx. This cascade reaction mechanism ensures sustained antibacterial action and accelerates wound healing. The results demonstrate that Q@CuMn@G exhibits the ability to effectively eliminate *E. coli* and *S. aureus* through generating •OH. Q@CuMn@G showed strong antibacterial activity both *in vitro* and *in vivo* settings, consumed glucose to produce oxygen, and improved the immune microenvironment of hypoxic and high-glucose in diabetic wounds, stimulated angiogenesis, and stimulated tissue regeneration. In conclusion, Q@CuMn@G shows significant potential in the treatment of diabetic bacterial infected wounds, providing an efficient, simple, and antibiotic-free antibacterial treatment strategy.

SUPPLEMENTARY MATERIAL

The comparison of the XRD patterns between Cu-MOF and simulated patterns, SEM images and elemental mapping of Q@CuMn@G, *in vitro* release behavior of Cu^{2+}, stability of GOx, and validation of the antibacterial mechanism involving hydroxyl radical generation by Q@CuMn@G are given in the supplementary material.

AUTHOR DECLARATIONS

Conflict of Interest

The authors have no conflicts to disclose.

Author Contributions

Yuxin Huang and Dixi Chen contributed equally to this work.

Yuxin Huang: Conceptualization (equal); Formal analysis (equal); Methodology (equal); Validation (equal); Writing – original draft (equal). **Dixi Chen**: Conceptualization (equal); Formal analysis (equal); Methodology (equal); Validation (equal). **T. M. Wong**: Investigation (equal); Visualization (equal). **Baolin Li**: Supervision (equal); Writing – review & editing (equal). **Yongxin Shi**: Project administration (equal); Supervision (equal); Writing – review & editing (equal).

DATA AVAILABILITY

The data that support the findings of this study are available from the corresponding authors upon reasonable request.

REFERENCES

[1] R. Nunan, K. G. Harding, and P. Martin, "Clinical challenges of chronic wounds: Searching for an optimal animal model to recapitulate their complexity," Dis. Models Mech. **7**(11), 1205–1213 (2014).

[2] A. Sood, M. S. Granick, and N. L. Tomaselli, "Wound dressings and comparative effectiveness data," Adv. Wound Care **3**(8), 511–529 (2014).

[3] T. Tuomi, N. Santoro, S. Caprio *et al.*, "The many faces of diabetes: A disease with increasing heterogeneity," Lancet **383**(9922), 1084–1094 (2014).

[4] V. Vijayakumar, S. K. Samal, S. Mohanty, and S. K. Nayak, "Recent advancements in biopolymer and metal nanoparticle-based materials in diabetic wound healing management," Int. J. Biol. Macromol. **122**, 137–148 (2019).

[5] H. C. Timmerhuis, F. F. van den Berg, P. C. Noorda *et al.*, "Overuse and misuse of antibiotics and the clinical consequence in necrotizing pancreatitis: An observational multicenter study," Ann. Surg. **278**(4), e812–e819 (2023).

[6] P. Manivasagan, T. Thambi, A. Joe *et al.*, "Progress in nanomaterial-based synergistic photothermal-enhanced chemodynamic therapy in combating bacterial infections," Prog. Mater. Sci. **144**, 101292 (2024).

[7] C. Jia, Y. Guo, and F. G. Wu, "Chemodynamic therapy via Fenton and Fenton-like nanomaterials: Strategies and recent advances," Small **18**(6), e2103868 (2022).

[8] Y. Shi, J. Yin, Q. Peng *et al.*, "An acidity-responsive polyoxometalate with inflammatory retention for NIR-II photothermal-enhanced chemodynamic antibacterial therapy," Biomater. Sci. **8**(21), 6093–6099 (2020).

[9] F. Li, M. Zang, J. Hou *et al.*, "Cascade catalytic nanoplatform constructed by laterally-functionalized pillar[5]arenes for antibacterial chemodynamic therapy," J. Mater. Chem. B **9**(25), 5069–5075 (2021).

[10] Z. Chen, Z. Wang, J. Ren, and X. Qu, "Enzyme mimicry for combating bacteria and biofilms," Acc. Chem. Res. **51**(3), 789–799 (2018).

[11] D. Kim, K. W. Park, J. T. Park, and I. Choi, "Photoactive MOF-derived bimetallic silver and cobalt nanocomposite with enhanced antibacterial activity," ACS Appl. Mater. Interfaces **15**(19), 22903–22914 (2023).

[12] X. Di, Z. Pei, Y. Pei, and T. D. James, "Tumor microenvironment-oriented MOFs for chemodynamic therapy," Coord. Chem. Rev. **484**, 215098 (2023).

[13] G. Xiang, B. Wang, W. Zhang *et al.*, "A Zn-MOF-GOx-based cascade nanoreactor promotes diabetic infected wound healing by NO release and microenvironment regulation," Acta Biomater. **182**, 245–259 (2024).

[14] S. Zulfiqar, S. Sharif, M. S. Nawaz *et al.*, "Cu-MOF loaded chitosan based freeze-dried highly porous dressings with anti-biofilm and pro-angiogenic activities accelerated *Pseudomonas aeruginosa* infected wounds healing in rats," Int. J. Biol. Macromol. **271**(Pt 2), 132443 (2024).

[15] F. Mo, S. Zhong, T. You *et al.*, "Aptamer and DNAzyme-functionalized Cu-MOF hybrid nanozymes for the monitoring and management of bacteria-infected wounds," ACS Appl. Mater. Interfaces **15**, 52114–52127 (2023).

[16] S. Chen, J. Chen, X. Wang *et al.*, "Glucose-activated self-cascade antibacterial and pro-angiogenesis nanozyme-functionalized chitosan-arginine thermosensitive hydrogel for chronic diabetic wounds healing," Carbohydr. Polym. **348**(Pt B), 122894 (2025).

[17] M. Cao, X. Xing, X. Shen *et al.*, "A review on nanomaterial-based strategies for manipulating tumor microenvironment to enhance chemodynamic therapy," Chem. Res. Chin. Univ. **40**(2), 202–212 (2024).

[18] L. Zhao, Y. Chen, Q. Wei *et al.*, "H_2O_2 self-supplied $CuFeO_x$ nanosystem as fenton-like reaction agents for endogenous/exogenous responsive synergetic antibacterial therapy," Chem. Eng. J. **492**, 152265 (2024).

[19] K. Wang, X. Wang, L. Zhang *et al.*, "Coordination-driven *in situ* grown copper peroxide in mesoporous dopamine with self-supplied H_2O_2 for synergistic enhanced PTT/CDT antibacterial treatment and wound healing," ACS Appl. Mater. Interfaces **16**(47), 64579–64591 (2024).

[20] H. Ma, Q. Yu, Y. Qu *et al.*, "Manganese silicate nanospheres-incorporated hydrogels:starvation therapy and tissue regeneration," Bioact. Mater. **6**(12), 4558–4567 (2021).

[21] J. Wang, L. Yao, E. Hu *et al.*, "MnO_2 decorated ZIF-8@GOx for synergistic chemodynamic and starvation therapy of cancer," J. Solid State Chem. **298**, 122102 (2021).

[22] L. Chen, S. Xing, Y. Lei *et al.*, "A glucose-powered activatable nanozyme breaking pH and H_2O_2 limitations for treating diabetic infections," Angew. Chem., Int. Ed. **60**(44), 23534–23539 (2021).

[23] Y. Wang, C. Li, B. Shen *et al.*, "Ultra-small Au/Pt NCs@GOX clusterzyme for enhancing cascade catalytic antibiofilm effect against *F. nucleatum*-induced periodontitis," Chem. Eng. J. **466**, 143292 (2023).

[24] K. Zhang, J. Wang, L. Peng *et al.*, "UCNPs-based nanoreactors with ultraviolet radiation-induced effect for enhanced ferroptosis therapy of tumor," J. Colloid Interface Sci. **651**, 567–578 (2023).

[25] S. Chen, Z. Hou, M. Xiao *et al.*, "Quaternized chitosan-based photothermal antibacterial hydrogel with pro-vascularization and on-demand degradation properties for enhanced infected wound healing," Carbohydr. Polym. **355**, 123350 (2025).

[26] J. Liu, D. Wu, N. Zhu *et al.*, "Antibacterial mechanisms and applications of metal-organic frameworks and their derived nanomaterials," Trends Food Sci. Technol. **109**, 413–434 (2021).

[27] X. Zhao, B. Guo, H. Wu *et al.*, "Injectable antibacterial conductive nanocomposite cryogels with rapid shape recovery for noncompressible hemorrhage and wound healing," Nat. Commun. **9**(1), 2784 (2018).

[28] Y. Feng, S. Qin, Y. Yang *et al.*, "A functional hydrogel of dopamine-modified gelatin with photothermal properties for enhancing infected wound healing," Colloids Surf., B **241**, 114058 (2024).

[29] P. R. Sarika and N. R. James, "Polyelectrolyte complex nanoparticles from cationised gelatin and sodium alginate for curcumin delivery," Carbohydr. Polym. **148**, 354–361 (2016).

[30] L. Huang, W. Li, M. Guo *et al.*, "Silver doped-silica nanoparticles reinforced poly (ethylene glycol) diacrylate/hyaluronic acid hydrogel dressings for synergistically accelerating bacterial-infected wound healing," Carbohydr. Polym. **304**, 120450 (2023).

[31] M. Wang, C. Wang, M. Chen *et al.*, "Efficient angiogenesis-based diabetic wound healing/skin reconstruction through bioactive antibacterial adhesive ultraviolet shielding nanodressing with exosome release," ACS Nano **13**(9), 10279–10293 (2019).

[32] L. Yang, F. Liang, X. Zhang *et al.*, "Remodeling microenvironment based on MOFs-Hydrogel hybrid system for improving diabetic wound healing," Chem. Eng. J. **427**, 131506 (2022).

[33] S. Chen, Y. Zhu, Q. Xu *et al.*, "Photocatalytic glucose depletion and hydrogen generation for diabetic wound healing," Nat. Commun. **13**(1), 5684 (2022).

[34] H. Wu, F. Li, W. Shao *et al.*, "Promoting angiogenesis in oxidative diabetic wound microenvironment using a nanozyme-reinforced self-protecting hydrogel," ACS Cent. Sci. **5**(3), 477–485 (2019).

[35] S. He, T. Walimbe, H. Chen *et al.*, "Bioactive extracellular matrix scaffolds engineered with proangiogenic proteoglycan mimetics and loaded with endothelial progenitor cells promote neovascularization and diabetic wound healing," Bioact. Mater. **10**, 460–473 (2022).

[36] J. U. Igietseme, Y. Omosun, T. Nagy *et al.*, "Molecular pathogenesis of *Chlamydia* disease complications: Epithelial-mesenchymal transition and fibrosis," Infect. Immun. **86**(1), e00585-17 (2018).